PASJ: Publ. Astron. Soc. Japan **60**, 961–974, 2008 October 25

Astrometry of H_2O Masers in Nearby Star-Forming Regions with VERA III. IRAS 22198+6336 in Lynds 1204 G

Tomoya HIROTA,[1,2] Kazuma ANDO,[3] Takeshi BUSHIMATA,[1,4] Yoon Kyung CHOI,[1] Mareki HONMA,[1,2] Hiroshi IMAI,[5] Kenzaburo IWADATE,[6] Takaaki JIKE,[6] Seiji KAMENO,[5] Osamu KAMEYA,[2,6] Ryuichi KAMOHARA,[1] Yukitoshi KAN-YA,[7] Noriyuki KAWAGUCHI,[1,2,4] Masachika KIJIMA,[2] Mi Kyoung KIM,[1,8] Hideyuki KOBAYASHI,[1,4,6,8] Seisuke KUJI,[6] Tomoharu KURAYAMA,[9] Seiji MANABE,[2,6] Makoto MATSUI,[3] Naoko MATSUMOTO,[2] Takeshi MIYAJI,[1,4] Atsushi MIYAZAKI,[6] Takumi NAGAYAMA,[3] Akiharu NAKAGAWA,[5] Daichi NAMIKAWA,[3] Daisuke NYU,[3] Chung Sik OH,[1,8] Toshihiro OMODAKA,[5] Tomoaki OYAMA,[1] Satoshi SAKAI,[6] Tetsuo SASAO,[9,10] Katsuhisa SATO,[6] Mayumi SATO,[1,8] Katsunori M. SHIBATA,[1,2,4] Yoshiaki TAMURA,[2,6] Kosuke UEDA,[3] and Kazuyoshi YAMASHITA[2]

[1]*Mizusawa VERA Observatory, National Astronomical Observatory of Japan, 2-21-1 Osawa, Mitaka, Tokyo 181-8588*
[2]*Department of Astronomical Sciences, Graduate University for Advanced Studies, 2-21-1 Osawa, Mitaka, Tokyo 181-8588*
[3]*Graduate School of Science and Engineering, Kagoshima University, 1-21-35 Korimoto, Kagoshima, Kagoshima 890-0065*
[4]*VSOP-2 Project Office, National Astronomical Observatory of Japan, 2-21-1 Osawa, Mitaka, Tokyo 181-8588*
[5]*Faculty of Science, Kagoshima University, 1-21-35 Korimoto, Kagoshima, Kagoshima 890-0065*
[6]*Mizusawa VERA Observatory, National Astronomical Observatory of Japan, 2-12 Hoshi-ga-oka, Mizusawa-ku, Oshu-shi, Iwate 023-0861*
[7]*Department of Astronomy, Yonsei University, 134 Shinchong-dong, Seodaemun-gu, Seoul 120-749, Republic of Korea*
[8]*Department of Astronomy, Graduate School of Science, The University of Tokyo, 7-3-1 Hongo, Bunkyo-ku, Tokyo 113-0033*
[9]*Korean VLBI Network, Korea Astronomy and Space Science Institute, P.O.Box 88, Yonsei University, 134 Shinchon-dong, Seodaemun-gu, Seoul 120-749, Republic of Korea*
[10]*Department of Space Survey and Information Technology, Ajou University, Suwon 443-749, Republic of Korea*
tomoya.hirota@nao.ac.jp

(Received 2008 April 28; accepted 2008 August 4)

Abstract

We present results of multi-epoch VLBI observations with VERA (VLBI Exploration of Radio Astrometry) of the 22 GHz H_2O masers associated with a young stellar object (YSO) IRAS 22198+6336 in a dark cloud, L 1204 G. Based on phase-referencing VLBI astrometry, we derived an annual parallax of IRAS 22198+6336 to be 1.309 ± 0.047 mas, corresponding to the distance of 764 ± 27 pc from the Sun. Although the most principal error source of our astrometry is attributed to the internal structure of the maser spots, we successfully reduced the errors in the derived annual parallax by employing position measurements for all of the 26 detected maser spots. Based on this result, we reanalyzed the spectral energy distribution of IRAS 22198+6336 and found that the bolometric luminosity and total mass of IRAS 22198+6336 are 450 $L_\odot$ and 7 $M_\odot$, respectively. These values are consistent with an intermediate-mass YSO deeply embedded in the dense dust core, which has been proposed to be an intermediate-mass counterpart of a low-mass Class 0 source. In addition, we obtained absolute proper motions of the H_2O masers for the most blue-shifted components. We propose that the collimated jets aligned along the east–west direction are the most plausible explanation for the origin of the detected maser features.

Key words: Astrometry — ISM: individual (Lynds 1204 G) — ISM: jets and outflows — masers (H_2O) — stars: individual (IRAS 22198+6336)

1. Introduction

One of the crucial issues in astronomy and astrophysics is to understand the formation processes of stars, planetary systems, and their clusters. They are the most basic constituents in the Galaxy, and hence play essential roles in its formation and evolution. In order to understand the physics and dynamics in the star-formation processes, it is necessary to obtain accurate physical properties of target sources, such as size, mass, and luminosity. Because all of these values strongly depend on the adopted distance, the distance is the most fundamental parameter for any quantitative discussion.

In spite of its importance, however, it has long been difficult to measure accurate distances to star-forming regions without assumptions. The most reliable and direct way to determine the distance is an annual trigonometric parallax method, based on precise measurements of the position and motion of the object. In the 1990's, the Hipparcos satellite measured annual parallaxes for more than 100000 stars with a typical precision of 1 mas level (Perryman et al. 1997). Nevertheless, accurate distance measurements with Hipparcos for star-forming regions were limited to nearby sources within a few hundred persec from the Sun (e.g., Lombardi et al. 2008). Although distances to several OB clusters associated with nearby star-forming regions up to ~ 600 pc have been reported (de Zeeuw et al. 1999), Hipparcos could not directly determine the distances to newly born stars deeply embedded in dusty molecular cloud cores, because Hipparcos was capable

of observing only in optical wavelengths.

In the last few years, phase-referencing VLBI astrometry has been developed drastically, yielding the annual parallaxes of nearby star-forming regions. For instance, radio continuum sources in the Taurus (Loinard et al. 2005, 2007; Torres et al. 2007), Ophiuchus (Loinard et al. 2008), and Orion (Sandstrom et al. 2007; Menten et al. 2007) regions were observed with the NRAO Very Long Baseline Array (VLBA) to derive their annual parallaxes with a typical uncertainty of better than a few percent.

In addition, we started the initial scientific project "Measurements of annual parallaxes of nearby molecular clouds" with VERA (VLBI Exploration of Radio Astrometry). VERA is a Japanese VLBI network dedicated to astrometric observations aimed at revealing the 3-dimensional structure of the Galaxy (Honma et al. 2007; Sato et al. 2007, 2008). In our project for nearby molecular clouds, we specially focus on accurate distance measurements of star-forming regions within 1 kpc from the Sun (Dame et al. 1987). Our results will contribute to refine all of the observational studies on nearby star-forming regions by providing their most accurate and directly measured distances. We have already conducted astrometric observations of the H_2O maser sources in Orion (Hirota et al. 2007), Ophiuchus (Imai et al. 2007), and Perseus (Hirota et al. 2008) regions. All of the results provide direct measurements of their distances with much higher accuracy than the previous photometric methods and parallax measurements with Hipparcos.

As a part of this project, we present results of astrometric observations of the H_2O maser source IRAS 22198+6336 in a nearby dark cloud core, Lynds 1204 G.[1] L 1204 is located in the Cepheus–Cassiopeia molecular cloud complex (Yonekura et al. 1997), and is associated with a well-known high-mass star-forming region, S 140. It is also identified to be a molecular cloud, WB 176 (Wouterloot & Brand 1989). According to molecular line observations of L 1204, it consists of several high-density molecular cores, labeled by A–G (Tafalla et al. 1993). A deeply embedded YSO IRAS 22198+6336 is associated with one of the dense cores, L 1204 G, and it is identified to be a powering source of molecular outflow (Fukui 1989; Wilking et al. 1989). The centimeter and millimeter counterparts of IRAS 22198+6336 were detected with the VLA (Sánchez-Monge et al. 2008). The H_2O masers were detected (Palla et al. 1991) and their distributions were investigated by the VLA (Tofani et al. 1995) and VLBA (Migenes et al. 1999). However, they did not measure the proper motions of the H_2O masers because observations by Tofani et al. (1995) could not achieve sufficient high resolution, and Migenes et al. (1999) observed only at 1 epoch. Therefore, the kinematics of the circumstellar materials around IRAS 22198+6336 still remains unclear.

The distance to L 1204 was estimated by a photometric method to be 910 pc (Crampton & Fisher 1974), assuming that a B0 V star, HD 211880, is the ionization source of the H II region S 140, which is also associated with L 1204. On the other hand, de Zeeuw et al. (1999), identified HD 211880 (HIP 110125) as a member of the Cepheus OB 2 cluster. Using the Hipparcos data, de Zeeuw et al. (1999) determined the distance to the Cepheus OB 2 cluster to be a closer value of 615 ± 35 pc from the Sun. A kinematic distance of 1.3 kpc was sometimes adopted in several papers (Wouterloot & Brand 1989; Molinari et al. 1996), according to a systemic velocity of $-11\,\mathrm{km\,s^{-1}}$ (Tafalla et al. 1993). Depending on the adopted distance, the luminosity of IRAS 22198+6336 could differ by a factor of 4, and hence its physical properties sometimes contain large uncertainties.

Based on our accurate astrometric observations with VERA, we will provide the parallactic distance to IRAS 22198+6336 in L 1204 G, together with the kinematics of the circumstellar gas traced by H_2O masers. We also discuss the basic properties of the powering source of the H_2O masers by adopting our new distance to L 1204 G.

2. Observations and Data Analysis

VERA observations of the H_2O masers (6_{16}–5_{23}, 22235.080 MHz) associated with IRAS 22198+6336 have been carried out since 2006 November at intervals of about 1 month, and are still ongoing. We present the results from a total of 9 observing sessions from 2006 November to 2007 December (2006/312, 2006/361, 2007/047, 2007/096, 2007/130, 2007/215, 2007/282, 2007/322, and 2007/353; hereafter an observing session is denoted by year/day of the year). All 4 VERA stations participated in all sessions, providing a maximum baseline length of 2270 km.

Observations were made in the dual-beam mode; the H_2O masers associated with IRAS 22198+6336 and a reference source J2223+6249 ($\alpha_{\mathrm{J2000.0}} = 22^{\mathrm{h}}23^{\mathrm{m}}18\overset{\mathrm{s}}{.}096661$, $\delta_{\mathrm{J2000.0}} = +62^{\circ}49'33\overset{''}{.}80393$; Petrov et al. 2005) were observed simultaneously (Kawaguchi et al. 2000; Honma et al. 2003, 2008a). The reference source, J2223+6249, is separated south from IRAS 22198+6336 by $1\overset{\circ}{.}1$. J2223+6249 was detected with a peak flux density of about 200 mJy in all the epochs, as shown in figure 1. Left-handed circular polarization was received and sampled with 2-bit quantization, and filtered using the VERA digital filter unit (Iguchi et al. 2005). The data were recorded onto magnetic tapes at a rate of 1024 Mbps, providing a total bandwidth of 256 MHz in which one IF channel and the rest of 15 IF channels with 16 MHz bandwidth each were assigned to IRAS 22198+6336 and J2223+6249, respectively. A bright continuum source, 3C 454.3, was observed every 80 minutes for bandpass and delay calibration. The system temperatures including atmospheric attenuation were measured with the chopper-wheel method (Ulich & Haas 1976) to be 100–500 K, depending on the weather conditions and the elevation angle of the observed sources. The aperture efficiencies of the antennas ranged from 45 to 52%, depending on the stations. A variation of the aperture efficiency of each antenna as a function of the elevation angle was confirmed to be less than 10%, even at the lowest elevation in the observations ($\sim 20^{\circ}$). Correlation processing was carried out on the Mitaka FX correlator (Chikada et al. 1991) located at the NAOJ Mitaka

[1] In some literature, IRAS 22198+6336 is called as L 1204 A (Fukui 1989; Palla et al. 1991; Migenes et al. 1999). However, it is quite confusing because L 1204 A is identified to be another core associated with the well known massive young stellar object (YSO) S 140 IRS 1 (Tafalla et al. 1993; Tofani et al. 1995). Thus, we refer to the host of IRAS 22198+6336 as L 1204 G in this paper according to Tafalla et al. (1993).

campus. For H_2O maser lines, the spectral resolution was set to be 15.625 kHz, corresponding to a velocity resolution of 0.21 km s^{-1}.

Data reduction was performed using the NRAO Astronomical Image Processing System (AIPS). Amplitude and bandpass calibrations were made for the H_2O maser source (IRAS 22198+6336) and reference source (J2223+6249) independently. For phase-referencing, fringe fitting was done with the AIPS task FRING on the phase reference source (J2223+6249), and the solutions were applied to the target source (IRAS 22198+6336). Because the reference source J2223+6249 showed a double-peaked structure in the synthesized images, as shown in figure 1, we carried out self-calibration to correct for the structure effect on the phase calibration. In addition, we applied the results of a dual-beam phase calibration, in which any differences between instrumentally added phases in the two beams were measured by injecting artificial noise sources into both beams at each station during the observations (Kawaguchi et al. 2000; Honma et al. 2008a). We also corrected for the approximate delay model adopted in the correlation processing. The difference in the optical path length error between our newly applied model and the CALC9 model developed by the NASA/GSFC VLBI group was confirmed to be less than $\sim$2 mm. In this correction, drifts of the visibility phase caused by the Earth's troposphere were estimated based on GPS measurements (Honma et al. 2008b). As discussed in Honma et al. (2008b), the tropospheric zenith delay consists of "dry" and "wet" parts, and only the latter one is variable, and hence significantly causes phase errors in the calibrations. The typical tropospheric "wet" zenith delay (path length) was 5–10 cm, while it was sometimes as large as 40 cm, particularly at the Ogasawara and Ishigaki stations during the summer. On the other hand, the "dry" component of the tropospheric zenith delay was stable at about 2.3 m.

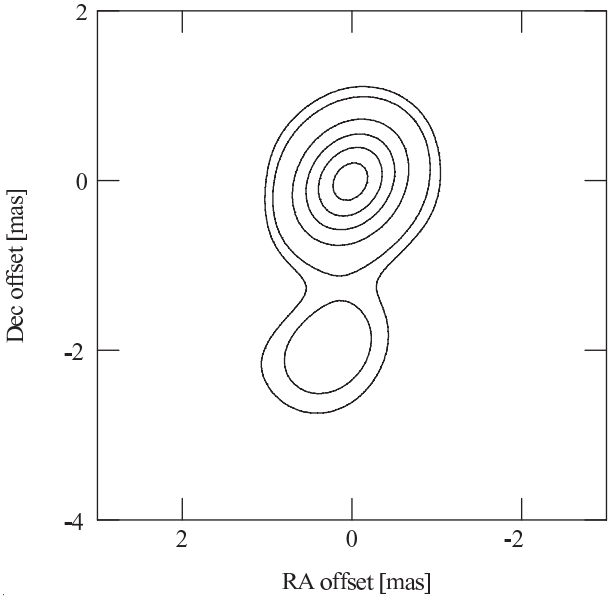

Fig. 1. Self-calibrated image of the reference source J2223+6249 at the first epoch, 2006/312. The contour levels are 5, 10, 30, 50, 70, and 90% of the peak intensity (205.3 mJy beam^{-1}).

Synthesis imaging and deconvolution (CLEAN) were performed using the AIPS task IMAGR with uniform weighting to achieve the highest spatial resolution, allowing us to resolve any complex spatial structures of the masers. The resultant synthesized beam size (FWMH) was typically 1.2 mas × 0.9 mas with a position angle of −40°. The peak positions and peak flux densities of masers were derived by fit ting elliptical Gaussian brightness distributions to each image using the AIPS task SAD. The formal uncertainties in the maser positions given by SAD were mostly better than 0.05 mas.

3. Results

3.1. Overall Properties of the H_2O Masers in L 1204 G

Figures 2 and 3 show an example of a total-power spectrum and scalar-averaged cross-power spectra of the H_2O masers associated with IRAS 22198+6336, respectively. The H_2O maser lines were detected within the LSR (local standard of rest) velocity range from −18.5 km s^{-1} to −2.7 km s^{-1}. The intense spectra at an LSR velocity of about −17 km s^{-1} were detected in all of the observed epochs, whereas other velocity components were detected at rarer occurrences. In this paper, we refer to the brightest components at −17 km s^{-1} as the main components. Our result is consistent with those of long-term monitoring observations made by Valdettaro et al. (2002) and Brand et al. (2003), that the most prominent maser feature in IRAS 22198+6336 was at an LSR velocity of about −20 km s^{-1}, while those around a systemic velocity of −11 km s^{-1} (Tafalla et al. 1993) rarely appeared. According to their long-term monitoring observations, the radial velocities of the H_2O masers in IRAS 22198+6336 changed with time over the 11 year monitoring period at a rate of 0.2 km s^{-1} yr^{-1}. The LSR velocity of the −20 km s^{-1} component has gradually been red-shifted to be about −18 km s^{-1} (Valdettaro et al. 2002; Brand et al. 2003). This trend predicts $\sim$−17 km s^{-1} of the velocity of the main component at around 2007, as observed in our observations. However, we cannot find any signature of the velocity drift within our observing period, probably due to our relatively shorter time span.

Since the spectrum taken at the first epoch, 2006/312, showed most of the velocity components, we first searched for the H_2O masers at the first epoch by producing the synthesized images for all of the individual velocity channels with a field of

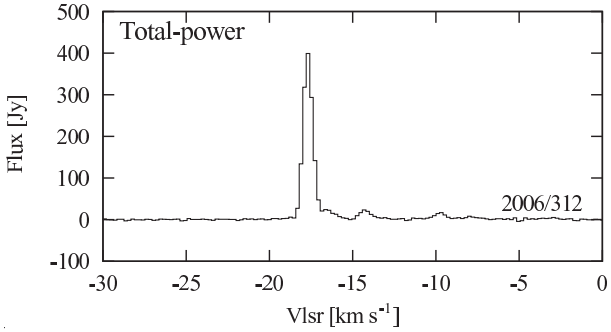

Fig. 2. Total-power spectrum of the H_2O masers associated with IRAS 22198+6336 observed at the first epoch, 2006/312. The spectrum is the average of those observed at all the VERA stations.

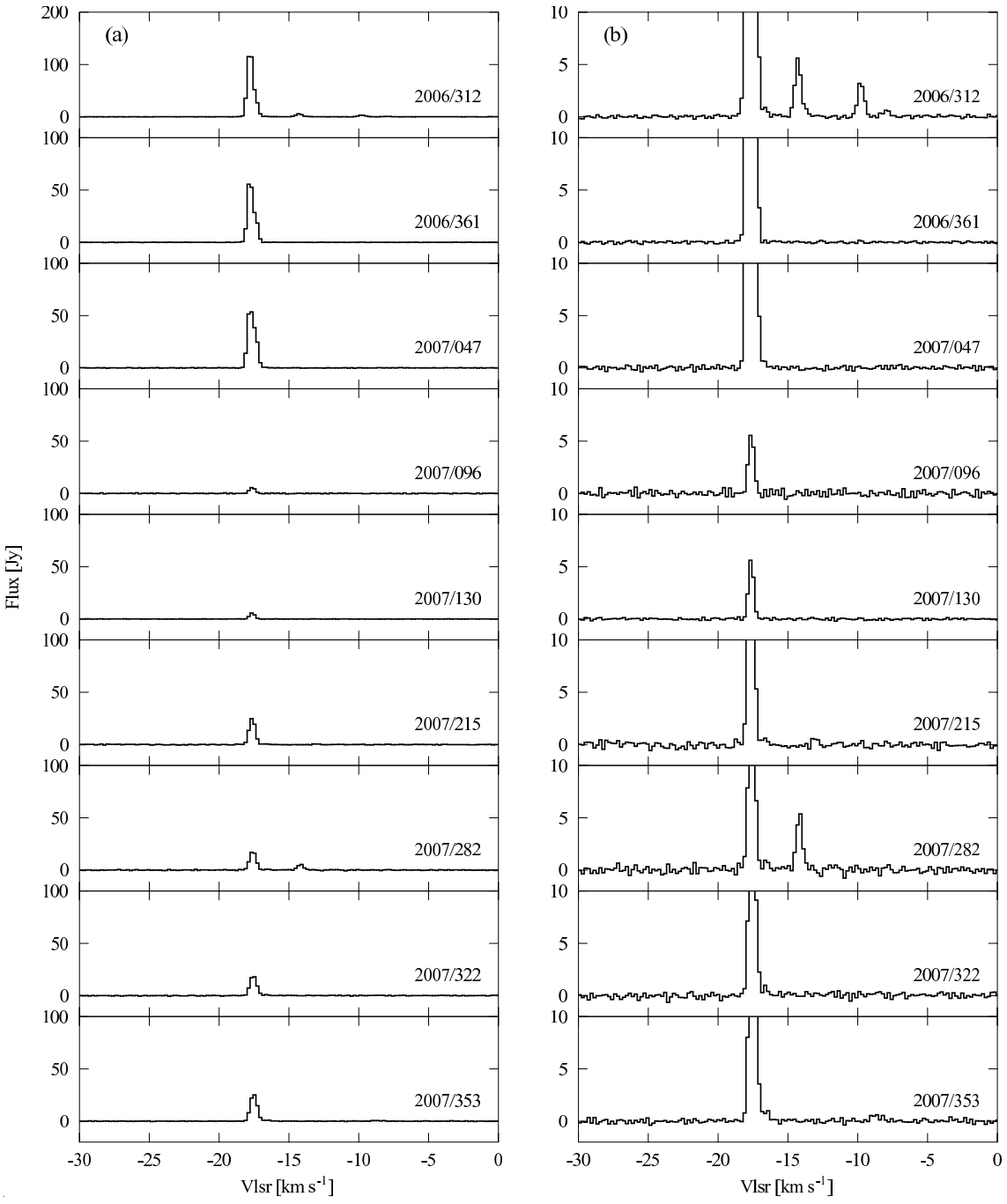

Fig. 3. (a) Scalar-averaged cross-power spectra of the H_2O masers associated with IRAS 22198+6336. The spectra are the averages of those observed at all VERA stations. Note that the scale of the ordinate for the 2006/312 epoch is twice as large as others. (b) Same as (a), but magnified by a factor of 10 to clarify the weaker spectral components.

view of $\sim 4'' \times 4''$. As a result, we found roughly 4 clusters of maser spots, or features, spreading over the 300 mas × 300 mas region. Hereafter, we define a "spot" as emission occurring in a single velocity channel and a "feature" as a group of spots that are spatially coincident within the beam size, and are detected for at least two consecutive velocity channels. Based on this coarse map, we again carried out synthesis imaging for all of the epochs with a field of view of 25.6 mas × 25.6 mas, centered at the positions for each of the identified features.

The results of the mapping are shown in figure 4, and examples of phase-referenced channel maps are shown in figure 5. We labeled the groups of features A–M in the order of their LSR velocities. Some of the weak components were not detected in the phase-referenced maps, but were only detected in the self-calibrated images. This is due to the lower dynamic range of the phase-referenced images than that of the self-calibrated images, in which we carried out phase-calibration using the brightest maser spot rather than the

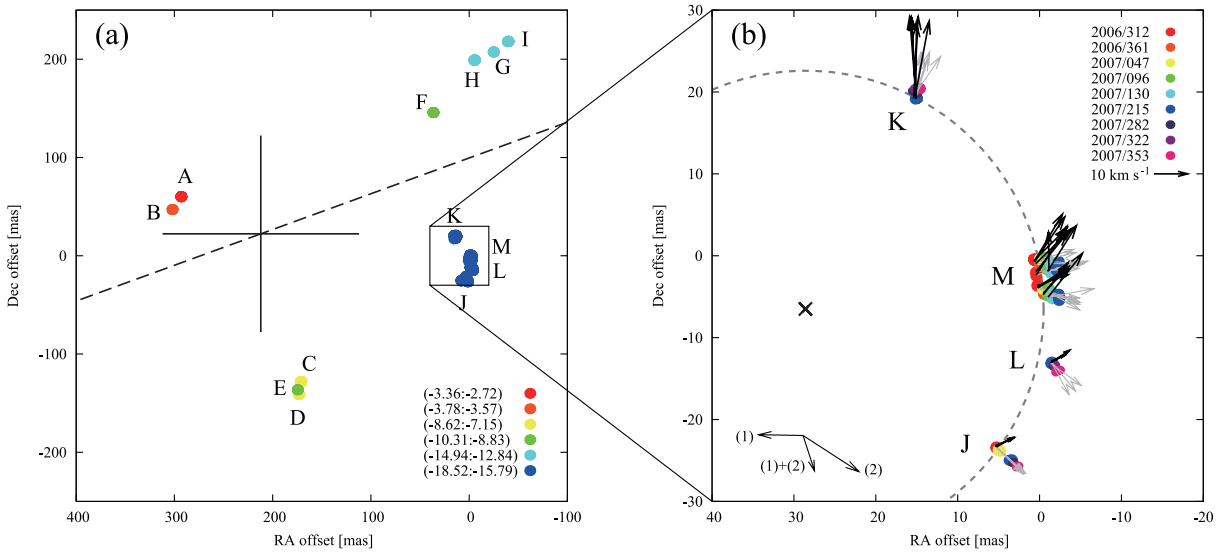

Fig. 4. Phase-referenced maps of the H_2O masers associated with IRAS 22198+6336. (a) Overall distribution of the H_2O maser spots. All of the detected spots for all of the 9 observing epochs are plotted. The position offsets in right ascension and declination were measured with respect to the (0,0) position at α (J2000.0) = $22^h21^m26^s.72790$, δ (J2000.0) = $+63°51'37''.9239$. A cross and a dashed line indicate the peak position and the direction of its elongation of the 7 mm radio continuum emission (Sánchez-Monge et al. 2008), of which the error bar was roughly estimated from the beam size and the signal-to-noise ratio of the VLA observation. (b) Distribution and proper motions of the maser spots in the main features, J–M. The movements of the spots indicated by the color-coded filled circles represent the absolute proper motions without any correction of the solar motion and galactic rotation. Gray arrows represent the absolute proper motions whereas the thick black arrows represent the proper motions, corrected for the solar motion and the galactic rotation. The proper motion of 1 mas yr^{-1} corresponds to 3.6 km s^{-1}, and the proper motion vector of 10 km s^{-1} is shown in the top-right corner of this figure. The arrows shown in the bottom-left corner represent the magnitude of (1) the solar motion (3.612 mas yr^{-1}, 0.064 mas yr^{-1}), (2) the galactic rotation (−4.543 mas yr^{-1}, −2.947 mas yr^{-1}), and the sum of (1) and (2). A large circle indicates the best-fit model of the possible expanding shell model (see text).

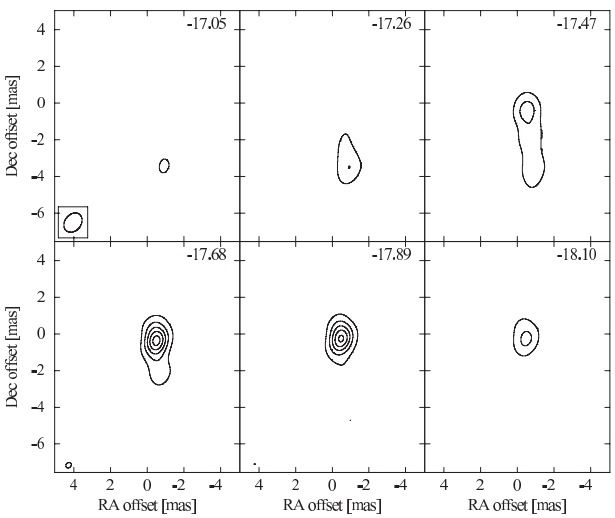

Fig. 5. Examples of phase-referenced channel maps of the elongated maser features M at the first epoch, 2006/312. The contour levels are 10, 30, 50, 70, and 90% of the peak intensity (112.2 Jy beam^{-1}). The LSR velocities are indicated at the top-right corner of each panel, in units of km s^{-1}. The beam size is shown in the top-left panel.

reference source J2223+6249. For such spots, we derived their absolute positions by referencing to the absolute position of the brightest spot in the main component, which is significantly detected in the phase-referenced images at all of the epochs.

The maser distribution shows roughly a circular structure with a radius of about 150 mas, as can be seen in figure 4a. The overall spatial and radial velocity distribution of the H_2O maser features are in good agreement with those by the VLA (Tofani et al. 1995) and the VLBA (Migenes et al. 1999), but we resolve the previously detected components into several spatially distinct maser spots due to our higher spatial resolution. The main components, which are the most blue-shifted and brightest, J–M, coincide with both the position and the velocity of the C2 component labeled by Tofani et al. (1995), while the most red-shifted components, A–B, coincide in the position and velocity with the C4 component of Tofani et al. (1995). The northern components near the systemic velocity, F–I, are also coincident with both the position and the velocity of the C1 component of Tofani et al. (1995). On the other hand, another group of components, C–E, is spatially coincident with C3 of Tofani et al. (1995), whereas their LSR velocities, from −7 to −10 km s^{-1}, are significantly red-shifted by more than 5 km s^{-1}. Here, we emphasize that the accuracy of our absolute positions with an uncertainty of only 1 mas, which is limited mainly by the position uncertainty of the reference source J2223+6249, 0.90 mas and 1.31 mas in right ascension and declination, respectively (Petrov et al. 2005), are about two orders of magnitude higher than those found by previous VLA observations (Tofani et al. 1995), and by fringe-rate maps obtained with VLBA (Migenes et al. 1999).

The properties of features A–I are summarized in table 1. These parameters were derived from the phase-referenced images, except for two features, D and E, as noted in table 1.

Table 1. The peak maser spots in the features A–I.*

No.	$v_{\rm lsr}$ [km s^{-1}]	Detected epoch	$\Delta\alpha$ [mas]	$\Delta\delta$ [mas]	$F_{\rm peak}$ [Jy beam^{-1}]
A	−3.15	2006/312	293.43	60.22	1.9
B	−3.57	2006/312	302.30	47.19	0.74
C	−8.20	2006/312	171.42	−128.00	3.9
D†	−8.41	2007/353	173.85	−141.05	2.2
E†	−8.83	2007/353	174.73	−136.19	2.7
F	−9.68	2006/312	36.88	145.81	11.5
G	−13.05	2007/215	−24.59	207.43	1.9
H	−14.31	2006/312	−5.22	199.21	15.7
I	−14.31	2007/353	−39.40	218.13	7.2

* Each feature is detected only at the epoch noted in the third column. The brightest spots in each feature are listed.
† The spots are detected only in the self-calibrated images.

Table 2. All of the maser spots in the main features J–M used for the parallax measurement.*

No.	$v_{\rm lsr}$ [km s^{-1}]	Detected epochs	$\Delta\alpha$ [mas]	$\Delta\delta$ [mas]	$F_{\rm peak}$ [Jy beam^{-1}]	$\mu_\alpha \cos\delta$ [mas yr^{-1}]	μ_δ [mas yr^{-1}]
J1	−16.42	1*3**67*9	4.15	−23.17	3.7	−2.33 (25)	−2.32 (32)
J2	−16.63	1*3**67*9	4.14	−23.31	6.4	−2.48 (25)	−2.20 (32)
J3	−16.84	1*3**67*9	4.03	−23.33	3.0	−2.27 (25)	−2.10 (32)
K1	−17.05	******789	14.21	20.60	2.7	−2.02 (168)	3.00 (213)
K2	−17.26	*****6789	15.53	20.48	4.7	−0.99 (83)	3.18 (105)
K3	−17.47	*****6789	15.51	20.44	8.2	−0.58 (83)	3.71 (105)
K4	−17.68	*****6789	15.48	20.46	8.5	−0.55 (83)	3.71 (105)
K5	−17.89	*****6789	15.51	20.46	6.8	−0.40 (83)	3.79 (105)
K6	−18.10	*****67*9	15.62	20.36	2.7	−1.29 (88)	3.80 (110)
L1†	−17.68	*****6789	−0.99	−11.88	12.8	−1.45 (83)	−2.63 (105)
L2†	−17.89	*****6789	−0.95	−11.94	10.1	−2.53 (83)	−1.85 (105)
L3†	−18.10	*****6789	−1.02	−11.77	2.5	−2.00 (83)	−2.44 (105)
M1	−17.05	123456***	−0.90	−3.40	19.6	−3.44 (41)	−2.00 (50)
M2	−17.26	123456***	−0.88	−3.37	60.2	−3.45 (41)	−1.23 (50)
M3	−17.47	123456***	−0.87	−3.53	48.8	−3.43 (41)	−1.35 (50)
M4	−17.68	*2*456***	−1.52	−5.48	10.4	−2.98 (55)	−0.75 (69)
M5	−17.89	*2*456***	−1.51	−5.47	8.9	−2.96 (55)	−0.26 (69)
M6	−18.10	***456***	−0.12	−5.75	0.6	−3.73 (98)	0.70 (125)
M7	−17.47	1**456***	−0.68	−1.82	42.6	−3.49 (45)	0.26 (55)
M8	−17.68	1**456***	−0.72	−2.28	20.4	−3.44 (45)	1.11 (55)
M9	−17.89	***456***	−0.08	−2.55	1.2	−3.28 (98)	0.83 (125)
M10	−18.10	*2*456***	−2.48	−2.67	3.3	−0.90 (55)	0.30 (69)
M11	−17.05	1*3**6***	−0.52	−0.35	2.7	−3.89 (45)	−0.01 (56)
M12	−17.68	1234*****	−0.50	−0.39	175.7	−3.39 (78)	0.80 (96)
M13	−17.89	12345****	−0.47	−0.22	146.1	−3.62 (60)	−0.24 (72)
M14	−18.10	1234*****	−0.45	−0.21	59.5	−3.24 (78)	0.99 (96)

* In the third column, the numbers indicate the detected epochs corresponding to 1: 2006/312, 2: 2006/361, 3: 2007/047, 4: 2007/096, 5: 2007/130, 6: 2007/215, 7: 2007/282, 8: 2007/322, and 9: 2007/353, respectively. The epoch in which the maser is not detected is indicated by an asterisk instead of above number. Positions and flux densities are those observed at the epoch detected for the first time, as noted in the third column. Numbers in parentheses represent the errors in units of the last significant digit.
† In the epochs of 2007/322 and 2007/353, the spots are detected only in the self-calibrated images.

They are compact and almost no significant spatial structures, and hence we only summarize the parameters for the peak spot in each feature. All of the features listed in table 1 were detected only at the epoch, recorded due to their high variability.

On the other hand, the brightest main features, J–M, show complex spatial structures. We summarize the parameters for the selected 26 spots in table 2, which were detected in at least three epochs, and hence, are usable to obtain reliable proper motions, as discussed later. The parameters for spots

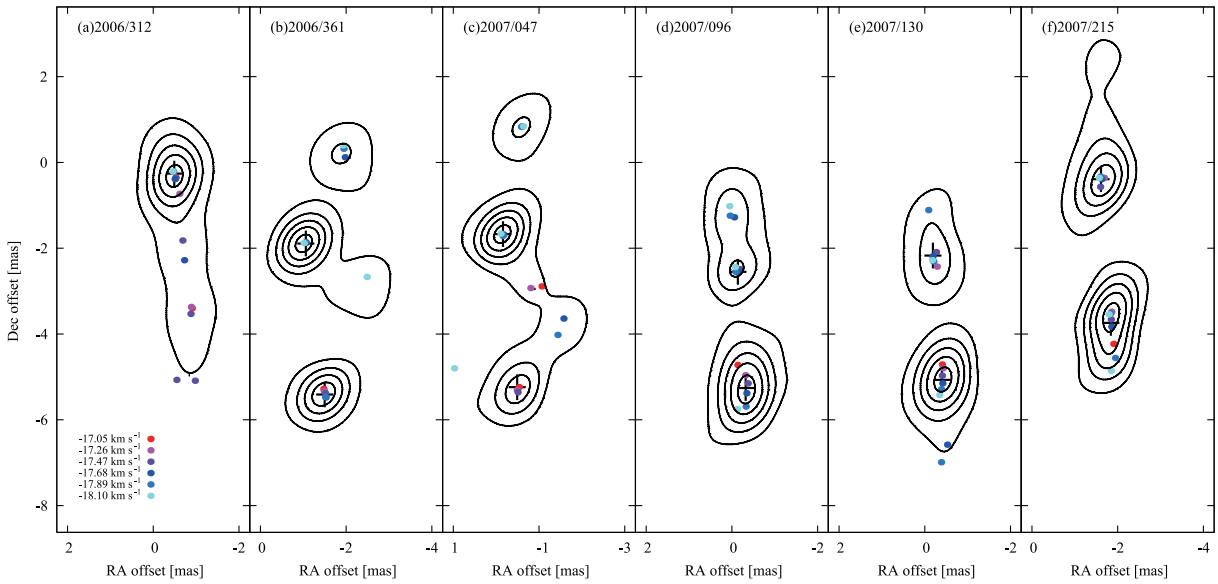

Fig. 6. Structures of the elongated maser features M obtained by integrating the phase-referenced channel maps. Contour maps show the integrated flux densities of the features with contour levels of 10, 30, 50, 70, and 90% levels of the peak flux densities. The peak values are 329.9 Jy beam^{-1}, 60.0 Jy beam^{-1}, 52.0 Jy beam^{-1}, 13.1 Jy beam^{-1}, 26.1 Jy beam^{-1}, and 16.2 Jy beam^{-1}, for (a)2006/312, (b)2006/361, (c)2007/047, (d)2007/096, (e)2007/130, and (f)2007/215, respectively. Crosses represent the positions and their error bars for the features employed in datasets 3 and 4 (see table 3), while color-coded filled circles represent the positions of the spots.

L1–3 were derived from self-calibrated images, while others are from the phase-referenced images. The main features were resolved into four subgroups: J (4 mas, −23 mas), K (15 mas, 20 mas), L (−1 mas, −12 mas), and M (−1 mas, −3 mas) in right ascension and declination, respectively, and all of them consist of multiple spots. In particular, the component M shows an elongated structure along the north–south direction from 0 mas to −6 mas in declination, as shown in figures 6 and 5. The relatively large-scale structures found in these features have been inferred from the fact that the H_2O masers are highly resolved-out with the longer baselines in the VLBA (Migenes et al. 1999). We also found that the flux densities of the cross-power spectra of the masers are typically only about 30% of those of the total-power spectra, as shown in figures 2 and 3, which are suggestive of the missing flux. Although the peak velocities of the main features, −17 km s^{-1}, were stable, their internal structures were found to be highly variable. Features K and L appeared later than 2007/215, while M was detected only at earlier epochs than 2007/215. In contrast, feature J was highly variable, but detected throughout the whole observing period.

As depicted in figure 4a, we found a radial velocity gradient along the east–west direction when we consider the clusters of features A–B and J–M; blue-shifted (J–M) and red-shifted (A–B) components tend to be distributed at the western and eastern sides of the map, respectively. The similar radial velocity gradient has been reported by Tofani et al. (1995) and Migenes et al. (1999), which is attributed to the bipolar outflow. On the other hand, the larger-scale ($> 1'$) velocity gradient along the northwest–southeast direction has been found in the spectral analysis (Jenness et al. 1995). Although they attributed these velocity gradients to the molecular outflow, their velocity structures showed an opposite trend to our H_2O maser distribution; the blue-shifted and red-shifted components traced by the NH_3 and $C^{18}O$ lines tend to be located at southeast and northwest, respectively. It would be suggested that the large-scale velocity gradient is not directly related to that traced by the H_2O masers. A detailed discussion about the spatial and velocity structures of the H_2O masers will be presented later.

3.2. *Astrometry of the H_2O Masers*

We conducted monitoring observations of H_2O masers for about one year, and their absolute motions were successfully obtained by referencing to the extragalactic position reference source J2223+6249. The movement of each maser spot can be expressed by the sum of a linear motion and the annual parallax. It can be assumed that all of the maser features or spots in L 1204 G have the same annual parallax within the astrometric accuracy of VERA. Therefore, we can simultaneously determine the proper motions ($\mu_\alpha^i \cos\delta$, μ_δ^i) and the initial positions (α_0^i, δ_0^i) in right ascension and declination for the i-th feature or spot, along with a common annual parallax of L 1204 G, π, by a least-squares analysis of all of the detected features or spots. Because only the features in the main components, J–M, were detected at more than two epochs, we excluded features A–I in the following astrometric analysis.

To obtain an accurate annual parallax, we attempted to analyze the data by adopting four different datasets: (1) both the right ascension and declination data for all of the spots, (2) only the right ascension data for all of the spots, (3) same as (1), but for all of the features, and (4) same as (2), but for all of the features. As already defined, the feature is the sum of the spatially coincident maser spots integrated over at least two consecutive velocity channels. Thus, we determined the peak position of each feature by a Gaussian fitting of the

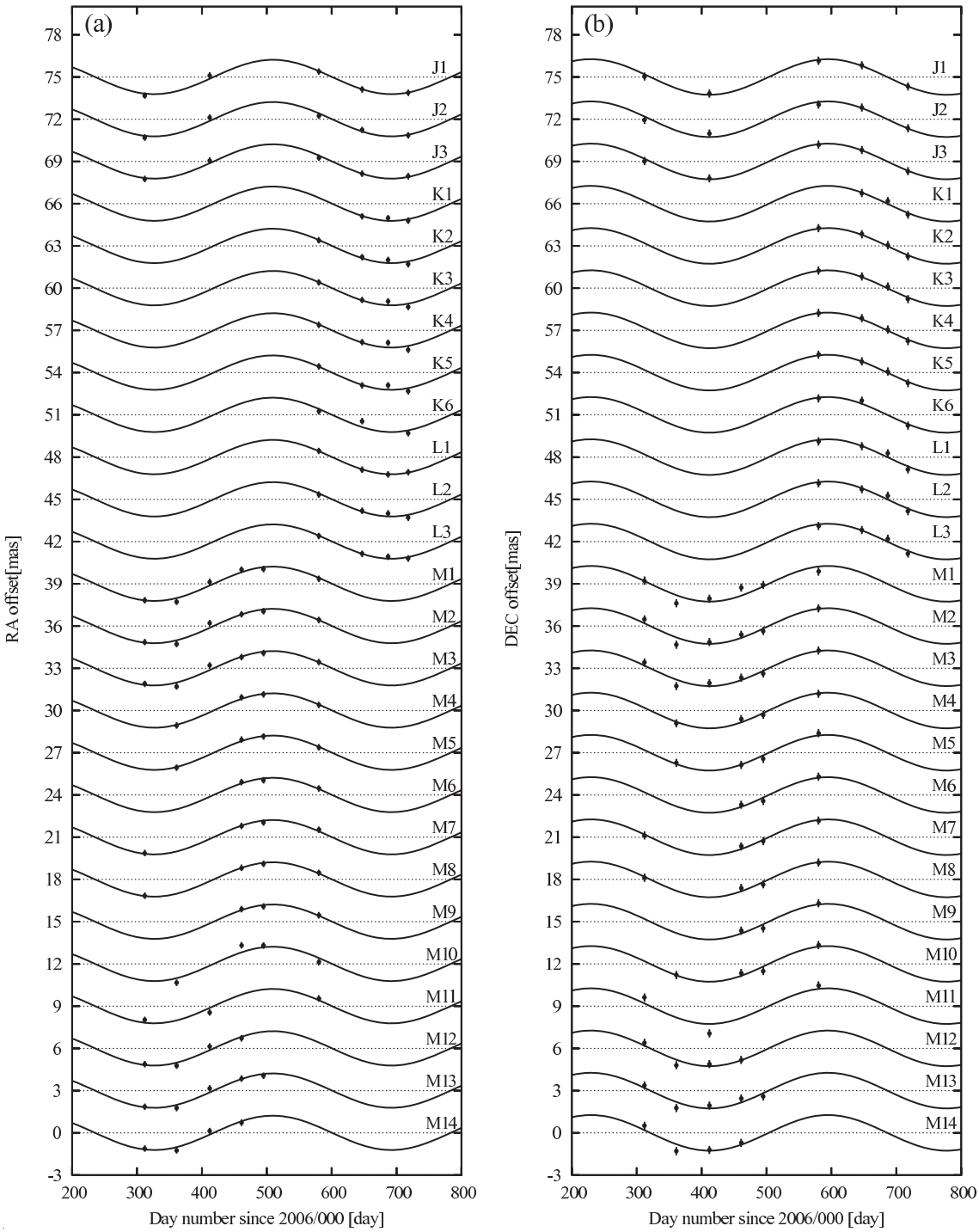

Fig. 7. Position measurements of the maser spots in the features J–M. (a) Movement in right ascension as a function of time. Solid lines represent the best-fit model of the annual parallax, which are common for all of the spots. The best-fit proper motions have been removed, and hence the curves represent the modulation in the positions due to the annual parallax. Filled circles represent the observed positions of the maser spots. (b) Same as (a) in declination. The associated error bars, 0.23 mas and 0.29 mas in right ascension and declination, respectively, are also plotted, but cannot be seen in the figures.

velocity-integrated phase-referenced intensity map. On the other hand, the peak position of each spot was derived from each individual channel map obtained from a phase-referenced analysis by assuming that the velocity of the maser spot is constant, i.e., the maser spots are regarded to be identical if their velocities are the same. This would not always be valid if the masers show a significant velocity drift (Hirota et al. 2008). However, we applied this assumption to indentity the detected spots between different epochs, because we could not find any significant velocity drift in our observations, as mentioned above.

A comparison of former and latter datasets shows the effect

Table 3. Summary of the least-squares analysis for the annual parallax measurements.*

Parameter	Dataset 1	Dataset 2	Dataset 3	Dataset 4
Dataset	RA and Dec 26 spots	RA only 26 spots	RA and Dec 5 features	RA only 5 features
Total number of data	218	109	52	26
Number of fitted parameters	105	53	21	11
Degree of freedom	113	56	31	15
π (mas)	1.309 (47)	1.289 (66)	1.243 (80)	1.288 (107)
D (pc)	764 (27)	776 (40)	805 (52)	777 (65)
σ_α (mas)	0.23	0.23	0.22	0.23
σ_δ (mas)	0.29	—	0.32	—

* Numbers in parentheses represent the errors in units of the last significant digit. σ_α and σ_δ are the rms deviations of the post-fit residuals in the right ascension and declination directions, respectively.

of the structures in the maser features on our astrometric accuracy. As mentioned above, we found significant spatial structures in features J–M. In particular, the elongated structure in feature M can be clearly seen in figure 6, in which the peak positions of the maser spots do not always coincide with those of the features. These complex spatial and velocity structures within the feature M would degrade the accuracy of astrometry, as reported in previous results of VERA for nearby sources (Hirota et al. 2007, 2008; Imai et al. 2007). Instead, we resolved the internal structure of feature M by producing channel maps of all of the velocity components. They could better trace the motion of the masing gas in the multi-epoch astrometric analysis. According to their positions and velocity channels, we identified in total 5 features (1 in features J–L for each and 2 in feature M) and 26 spots in the main components J–M, as listed in table 2, which were detected in at least three observing epochs. Some of the spots, for instance, the spots J1–3, K6, M4–5, M7–8, and M10–11, were not always detected, probably due to the variability and the insufficient sensitivity. However, our identification of the maser spots has proved to be appropriate, because their motions are well fitted to the linear proper motions and annual parallax, which is common for other spots, as shown in figure 7. Thus, all of the proper motions identified in our analysis really trace the bulk motion of the masing gas.

In addition, we evaluated the effect of the atmospheric zenith delay residual by comparing datasets 1 and 3 with those of datasets 2 and 4. According to previous results with VERA (Honma et al. 2007; Hirota et al. 2007, 2008; Imai et al. 2007), the accuracy of the derived annual parallax is significantly improved when only the data for right ascension are used, because this data is less affected by atmospheric modeling errors. Therefore, we ran the fitting by making use of right-ascension data alone, and both right ascension and declination data for a comparison.

All of the results for four different datasets can be compared in table 3. The results of the fitting are also displayed in figure 7 for dataset 1. The standard deviations of the post-fit residuals are ~ 0.2 mas and ~ 0.3 mas in right ascension and declination, respectively. If we employ the formal uncertainties in the Gaussian fitting of the maser spots, ~ 0.05 mas, as the positional errors in our observations, a reduced-χ^2 is as large as 20. This result would suggest that we have underestimated the positional errors, and that these post-fit residuals represent the actual positional accuracy of astrometric observations with VERA. Thus, we took into account both σ_α and σ_δ listed in table 3 in the least-squares analysis to give a weight, which is inversely proportional to the square of the error, for the right ascension and declination data, respectively.

As can be seen in table 3, all of the 4 datasets yield consistent parallax values within the mutual errors. Although none of the spots were persistent during the whole observing period, due to their variability, we could determine the annual parallax with an uncertainty of smaller than 10% by successfully identifying multiple spots during almost 1 year. The highest accuracy is achieved by adopting both right ascension and declination data for all of the 26 detected spots, dataset 1. The resultant value of the annual parallax for the dataset 1 is 1.309 ± 0.047 mas, corresponding a distance to IRAS 22198+6336 of 764 ± 27 pc. The associated uncertainties of only $\sim 4\%$ for the dataset 1 are smaller than the others, and this dataset provides the most reliable value. Detailed discussions about the possible astrometric error sources are presented in the subsection 4.1.

Along with the annual parallax, the proper motions of the maser spots were derived, as summarized in table 2, and illustrated in figure 4b. The proper motion of 1 mas yr^{-1} corresponds to 3.6 km s^{-1} at a distance of 764 pc. Although the proper motions for some of the features contain large uncertainties, we can see a systematic trend in the direction and magnitude of the proper-motion vector in figure 4b. The kinematics traced by the proper motions as well as the radial velocities of the masers are discussed in subsection 4.4.

4. Discussions

4.1. Astrometric Error Sources

As discussed in recent studies on astrometry with VLBA and VERA (Hachisuka et al. 2006; Honma et al. 2007), it is difficult to estimate individual error sources induced in VLBI astrometry quantitatively. We regard the post-fit residuals of the least-squares analysis listed in table 3 as being typical positional errors, which results in a reduced-χ^2 of unity. Because they are significantly larger than the formal uncertainties in the Gaussian fitting of the maser spots, ~ 0.05 mas, some systematic errors would have significant effects on the astrometry. Here, we discuss the possible error sources in the present results.

One of the serious error sources is the atmospheric zenith delay residuals mainly due to the tropospheric water vapor. This effect is caused by the difference in the optical path lengths through the atmosphere between the target and reference sources, because their elevation angles are usually different. Honma et al. (2008b) presented results of detailed simulations to calculate the positional errors caused by the atmospheric zenith delay residuals in astrometry with VERA. They demonstrated that the positional error due to the zenith delay residual of 2 cm, which is a typical value of VERA observations, is better than 0.030 mas and 0.018 mas for right ascension and declination, respectively, in the case of a declination of 60°, the separation angle (SA) between the two sources of 1°, and the position angle (PA) on the sky from the target source to the reference source of 180°, which are valid for the IRAS 22198+6336 and J2223+6249 pair aligned along the north–south direction. It turns out that the simulated positional error for this pair cannot fully explain the observed positional uncertainties, unless we introduce an unrealistically large scatter of the zenith delay residual of ~ 30 cm for each observation. Therefore, it is unlikely that the atmospheric zenith delay residuals are the most dominant sources of our astrometric errors.

Alternatively, we propose that the principal error source in the present results would be the temporal variation of the internal structure of the masers, as proposed by some previous results from the VERA astrometry (Hirota et al. 2007, 2008; Imai et al. 2007). This effect would be more serious for nearby sources than the distant ones. In fact, we can see the spatial structure of the features in figure 6, and some of the spots in figure 7 show significant deviations from the best-fit model. Even in the case of the fitting of the spots, rather than the features, the internal structures in the individual spots might still be significant. Although this effect would limit the positional accuracy of each observation, the accuracy of the annual parallax measurements can be improved with increasing the number of spots used in the analysis if the variation of the structure behaves in a random way. Indeed, the post-fit residuals are reduced almost inversely in proportion to the square root of the degrees of freedom in the fitting, as listed in table 3.

On the other hand, we confirmed that the uncertainties in the station positions, path-length errors due to the ionosphere, and the delay model employed in our data analysis, which is consistent with the CALC9 model, would have negligible effects on our astrometry with VERA (Honma et al. 2007). The uncertainties in the absolute position of the reference source J2223+6249, 0.90 mas and 1.31 mas in right ascension and declination, respectively (Petrov et al. 2005), do not affect the derived annual parallax and proper motion because they would add only a constant offset to the position of the maser features. The spatial structure and its temporal variation of the reference source J2223+6249 possibly contribute to the positional errors of the maser features. However, the structure effect of the reference source would be much less significant than those of the masers, because we performed self-calibration of J2223+6249 to solve its structure. According to the dynamic range of the self-calibrated image of J2223+6249 (~ 20: figure 1), the positional uncertainty caused by the structure of the reference source would be less than 0.025 mas (HPBW/2SNR, where HPBW and SNR represent the synthesized beam width and the signal-to-noise ratio, respectively).

In summary, we conclude that the astrometric accuracy in our observations is mainly limited by the structure of the maser features, and that the atmospheric zenith delay residuals also contribute to some extent to the error sources. As suggested by Honma et al. (2008b), the tropospheric zenith delay residual also acts as a random error, because they are correlated only over a few days. Thus, one can reduce the post-fit residuals by employing longer observing epochs as well as using a larger number of masers. Thus, longer monitoring observatios will be helpful to achieve higher precision and accuracy of the parallax measurements, which are still underway.

4.2. *Distance to IRAS 22198+6336 in L 1204 G*

We derived the distance to L 1204 G to be 764 ± 27 pc from the Sun. This value is smaller than the earlier photometric result, 910 pc (Crampton & Fisher 1974), and the kinematic distance, 1.3 kpc (Wouterloot & Brand 1989; Molinari et al. 1996). While they did not report the errors in the derived distances, the photometric and kinematic distances would generally contain larger uncertainties by a factor of a few tens of percent than the parallactic distances (e.g., Hirota et al. 2008; Sato et al. 2008, and references therein). The closer distance, 615 ± 35 pc, is reported by de Zeeuw et al. (1999) based on Hipparcos measurements of the annual parallaxes of the Cepheus OB 2 cluster members, in which one of the members, HD 211880, is the ionization source of S 140 which is possibly associated with L 1204. This value is offset from our measured distance of IRAS 22198+6336 by 149 ± 44 pc, and is slightly larger than the apparent diameter of the Cepheus OB 2 cluster of about 130 pc ($\sim 12°$ on the celestial sphere: de Zeeuw et al. 1999). If L 1204 G is physically associated with the Cepheus OB 2 cluster, our result suggests that L 1204 G would be located at the farthest side of the Cepheus OB 2 cluster. Our parallactic distance to IRAS 22198+6336 is found to be very close to the well-studied H_2O maser sources in the Cepheus–Cassiopeia region, such as IC 1396 N (Patel et al. 2000) and Cepheus A (Torrelles et al. 2001), although they are not based on parallax measurements. Together with the parallactic distances of the maser sources in this region including NGC 281, reported by Sato et al. (2008), and further measurements, such as for IC 1396 N and Cepheus A, we will be able to reveal the 3-dimensional structure of this molecular cloud complex and refine statistical studies of star-formation in this region (Yonekura et al. 1997).

4.3. *Physical Properties of IRAS 22198+6336*

Although the adopted FIR luminosity of IRAS 22198+6336 is different from literature to literature, it has been included in the sample of massive YSOs, judging from the relatively large far-infrared or bolometric luminosity (Palla et al. 1991; Molinari et al. 1996; Sánchez-Monge et al. 2008). For instance, Tafalla et al. (1993) adopted $L_{\rm IRAS}$ to be $250\,L_\odot$, while Tofani et al. (1995) adopted $L_{\rm FIR}$ to be $580\,L_\odot$ by assuming the same distance of ~ 900 pc. In contrast, Molinari et al. (1996) assumed a kinematic distance of 1.3 kpc, and derived a larger FIR luminosity of $1240\,L_\odot$. Very recently, Sánchez-Monge et al. (2008) reported results of a survey of

millimeter and centimeter continuum emission from high-mass to intermediate-mass YSOs, including IRAS 22198+6336, of which they adopted a luminosity of 1300 $L_\odot$. Based on radio continuum observations with the VLA of IRAS 22198+6336 along with the observed flux densities reported in previous literature, Sánchez-Monge et al. (2008) presented basic physical properties of the radio counterpart of the IRAS source, VLA 2, such as the mass and the luminosity.

However, all of these results employed larger distances than our present result. Here, we refine the physical properties of the possible powering source of the H_2O masers, IRAS 22198+6336 VLA 2, based on our newly derived distance and previously reported flux values by multiplying a scaling factor proportional to an appropriate power of the distance D. For instance, a factor of $(764\,\mathrm{pc}/1300\,\mathrm{pc})^2 = 0.35$ is adopted for correcting the luminosity reported by Sánchez-Monge et al. (2008).

First of all, we stress that the bolometric luminosity is reduced to be 450 $L_\odot$, which is only 35% of previously adopted value, 1300 $L_\odot$. Such a low luminosity would argue against a classification of IRAS 22198+6336 as being a massive YSO. The derived luminosity sets limits on the stellar mass of IRAS 22198+6336. If it is a zero-age main sequence (ZAMS) star, the spectral type of late-B (between B6 and B7) with a stellar mass of about 5 $M_\odot$ (Stahler & Palla 2004) well accounts for the derived luminosity. On the other hand, if it is in a pure accretion phase, the stellar mass of 7 $M_\odot$ is derived from the accretion luminosity with a typical mass accretion rate of $10^{-5} M_\odot\,\mathrm{yr}^{-1}$ and a stellar radius of 5 R_* (Stahler & Palla 2004). The newly obtained total (gas+dust) mass of IRAS 22198+6336, (7–10) $M_\odot$, which is only 35% of that derived from the SED (spectral energy distribution) fitting (Sánchez-Monge et al. 2008), is in good agreement with the above values. Thus, our result implies that IRAS 22198+6336 is not a massive, but an intermediate-mass YSO with a mass of no more than 7 $M_\odot$. The lack of the IRAS 12 μm emission as well as no near-infrared counter part in the 2MASS images support the hypothesis that IRAS 22198+6336 is a deeply embedded intermediate-mass YSO, which is analogous to a low-mass Class 0 source (Sánchez-Monge et al. 2008).

According to Sánchez-Monge et al. (2008), IRAS 22198+6336 is associated with centimeter radio continuum emission, which could arise either in an ultra-compact H II region, or a shock-ionized region in the outflow. They concluded that the contribution of shock-ionized gas around IRAS 22198+6336 should be only a small fraction of the observed centimeter emission because of an extremely high ratio of the centimeter continuum luminosity, $S_\nu D^2$, to the outflow momentum rate, $\dot{P}$, with an efficiency factor of 90%. However, if we assume distance of 764 pc, the ratio is reduced by a factor of 0.59, because the luminosity is proportional to D^2, while the outflow momentum rate, which is usually derived from the linear size, radial velocity, and inclination angle of the outflow, is proportional to D. Even if this is the case, the efficiency of 50% is still higher than the typical low-mass YSOs, $\sim$10% (Anglada 1995), suggesting that it would be significantly higher in the very early stage of intermediate-mass YSOs.

The mass and luminosity of IRAS 22198+6336, refined by our newly derived distance, is consistent with that of the intermediate-mass deeply embedded YSO with the spectral type of late-B. The nondetection of 6.7 GHz CH_3OH masers, which are thought to be signposts of massive star-formation sites, toward IRAS 22198+6336 (Szymczak et al. 2000) also supports our conclusion that IRAS 22198+6336 is not a massive YSO. Although OH masers, which is another signature of massive star-formation associated with an ultra-compact H II region, are detected toward IRAS 22198+6336 (Edris et al. 2007), a relatively lower resolution of the OH maser observations, $\sim 3'$, might give argument against their association with the same powering source of the H_2O masers. Further observational studies with higher resolution and higher sensitivity centimeter, millimeter, and submillimeter interferometers would shed light on the properties of the central star in L 1204 G more clearly. Such detailed observational studies on IRAS 22198+6336 would be quite important, because it is one of the rare sources in the very early stage of an intermediate-mass YSO associated with H_2O masers (e.g., Patel et al. 2000), and hence good target sources for a complete understanding of the very early stage of intermediate-mass star-formation processes.

4.4. *Kinematics of the Jet Traced by the H_2O Masers in IRAS 22198+6336*

Together with the annual parallax, we successfully measured the proper motions of the maser spots around IRAS 22198+6336. These results enable us to discuss in detail about the kinematics of the circumstellar materials. Prior to discussions, we should note that the proper motions obtained with VERA do not represent the "intrinsic" proper motions of the masers, because they were measured with respect to the Sun, and hence include the contribution of the solar motion and the galactic rotation. Assuming the solar motion relative to the LSR based on the Hipparcos satellite data, $(U_0, V_0, W_0) = (10.00, 5.25, 7.17)\,\mathrm{km\,s^{-1}}$ (Dehnen & Binney 1998), we estimated the contribution of the solar motion to the observed absolute proper motion to be $3.612\,\mathrm{mas\,yr^{-1}}$ and $0.064\,\mathrm{mas\,yr^{-1}}$ in right ascension and declination, respectively. In addition, the contributions of the galactic rotation were calculated to be ($-4.543\,\mathrm{mas\,yr^{-1}}$, $-2.947\,\mathrm{mas\,yr^{-1}}$) based on the assumption of flat rotation with an R_0 of 8.0 kpc (Reid 1993) and a Θ_0 of $236\,\mathrm{km\,s^{-1}}$ (Reid & Brunthaler 2004) for L 1204 G at a distance of 764 pc. Subtracting these values from the observed proper motions listed in table 3 and shown in figure 4b, we obtained the intrinsic proper motions of the H_2O masers corrected for the solar motion and the galactic rotation.

The origin of these proper motions is attributed to either the systemic motion of the host cloud, L 1204 G, itself, the internal motions of the masers with respect to the powering source IRAS 22198+6336, such as jets and rotating disk associated with it, or both. Regarding the systemic motion, the observed proper motions might trace the peculiar motion of L 1204 G with respect to the galactic rotation. The discrepancy between the kinematic distance of L 1204 G, which was obtained by assuming that L 1204 G exactly followed the galactic rotation curve, and our parallactic distance would be suggestive of the effect of the peculiar motion of L 1204 G, rather than the galactic rotation. Indeed, L 1204 G ($b \sim 5.^\circ7$) was situated at 75 pc above the galactic plane with a half-thickness of 87 pc

(Dame et al. 1987), which seems to be too large to apply the flat rotation model. However, the systemic motion of L 1204 G is quite uncertain because of a lack of proper-motion measurements of IRAS 22198+6336, as suggested in the previous result with VERA of NGC 1333 (Hirota et al. 2008). Therefore, here we only consider several possibilities for the origin of the internal proper motions of the masers and the kinematics in the circumstellar material.

As shown in figure 4a, the proper motions of features J–M provide a hint of systematic motion directed outward from the center of the circular structure with an approximate diameter of $\sim$300 mas, or 200 AU. It is naturally interpreted that the most blue-shifted and red-shifted components trace the interacting region with the ambient gas and the collimated jets aligned in the east–west direction, and that the powering source is located at the center of the maser distribution (see figure 4a). This is roughly consistent with the position and elongation of the VLA source observed at the 7 mm band (Sánchez-Monge et al. 2008), although their spatial resolution is much larger than our VLBI observations. The possible trend of the northward proper motion vectors in figure 4b could be due to some unknown systemic motion of the powering source. A close-up view of the main features shows an arc-like structure, indicative of a bow shock, as can be seen in figure 4b. Such bow-shock structures at the tips of the collimated jets have been found in low-mass Class 0 protostars, IRAS 05413−0104 (Claussen et al. 1998) and S 106 FIR (Furuya et al. 2000).

In this case, the origin of the other maser spots close to the systemic velocity, which seem to be distributed perpendicular to the possible jets, would be accounted for by the rotating disk. The radial velocity difference along the north–south direction, $\sim 8\,\mathrm{km\,s^{-1}}$ and their separation, $\sim$200 AU ($\sim$300 mas), implies Keplerian rotation with a centrally enclosed mass of $1.6\,M_\odot/\cos^2 i$, where i is the inclination angle between the rotation axis and the line-of-sight. The inclination angle of disk i can be estimated from that of the east–west jets traced by the most blue-shifted and red-shifted masers, as follows. The mean proper motions of the most blue-shifted masers are derived to be $-1.53\,\mathrm{mas\,yr^{-1}}$ and $3.15\,\mathrm{mas\,yr^{-1}}$ in right ascension and declination, respectively. If we adopt the proper motions only in the right ascension direction as the outward velocity of the jets, the mean transverse velocity of $5.5\,\mathrm{km\,s^{-1}}$ toward west and the mean radial velocity of $-6.6\,\mathrm{km\,s^{-1}}$ with respect to the systemic velocity for the maser spots J–M give an inclination angle, i, of 50°. Similarly, if we adopt the proper motions of both the right ascension and declination direction, the mean transverse velocity of $12.6\,\mathrm{km\,s^{-1}}$ yields an inclination angle, i, of 66°. The enclosed mass is estimated to be $3.9\,M_\odot$ and $9.7\,M_\odot$ for former and latter cases, respectively, and these values are almost consistent with the result of the SED fitting, $\sim 7\,M_\odot$.

On the other hand, the radio continuum emission in the 1.3 cm and 7 mm bands showed an elongated structure along the northwest–southeast direction (Sánchez-Monge et al. 2008). According to their SED analysis, the 1.3 cm emission is dominated by the free–free emission from the shock-ionized jets, while 44% of the 7 mm flux comes from thermal dust emission in the circumstellar disk, and hence the 7 mm emission would be due to a superposition of the ionized jet and the dust disk (Sánchez-Monge et al. 2008). Because the directions of the radio continuum emissions are consistent with that of the large-scale velocity gradient (Tafalla et al. 1993; Jenness et al. 1995), Sánchez-Monge et al. (2008) attributed them to free–free emission from the ionized radio jets. However, the large-scale velocity gradient showed an opposite trend to our H_2O maser distribution, as mentioned in subsection 3.1. The maser distributions might trace an interface between the ambient material and the outflow lobe that is parallel to the radio continuum source (e.g., Moscadelli et al. 2006), whereas the asymmetric distribution of the masers with respect to the outflow axis cannot be accounted for by only the simple model.

It is worth considering another possibility of the rotating disk around the YSO with a rotation axis along the north–south direction. If we assume the radial velocity gradient along the east–west direction, $\sim 16\,\mathrm{km\,s^{-1}}$ per $\sim$ 200 AU ($\sim$300 mas), as a cause of rotation, the enclosed mass is estimated to be at least $6.4\,M_\odot$, which is comparable to the total mass or stellar mass of IRAS 22198+6336, as discussed in the previous section. In this case, the northern and southern components C–I would trace the jets from the central YSO. Their radial velocity close to the systemic velocity would indicate that the jets are aligned almost within the plane of the sky, and hence the disk is almost an edge-on view. The directions of the radio continuum emissions in the 1.3 cm and 7 mm bands (Sánchez-Monge et al. 2008) are in good agreement with that of the H_2O maser features C–I. Nevertheless, this model cannot explain the observed velocity drift of $0.2\,\mathrm{km\,s^{-1}\,yr^{-1}}$ for the $-20\,\mathrm{km\,s^{-1}}$ feature (Valdettaro et al. 2002; Brand et al. 2003), because the velocity drift at the edge of the disk (at the radius of 100 AU) is estimated to be only $0.01\,\mathrm{km\,s^{-1}\,yr^{-1}}$ in the case of the YSO with a mass of $5\,M_\odot$. Thus, the rotating disk with the axis in north–south direction is inadequate to explain the kinematics in the circumstellar materials around IRAS 22198+6336 probed by the blue-shifted maser features J–M.

Alternatively, the distributions and proper motions of features J–M could also be interpreted as being a part of a smaller scale expanding shell, as shown in figure 4b, with a radius of 29.1 ± 0.8 mas (22.2 ± 0.6 AU) and an expanding velocity of $3.8 \pm 0.4\,\mathrm{km\,s^{-1}}$ in the plane of the sky. In this case, the dynamical time of the expanding shell is calculated to be only 8 years. The basic characteristics of this expanding shell is quite similar to the case of Cepheus A (Torrelles et al. 2001) and W 75 N (Torrelles et al. 2003). Meanwhile, the nature of the possible powering source of the shell is not consistent with the position and elongation of the radio continuum emission (Sánchez-Monge et al. 2008). In addition, it is unlikely that such a shell is traced only by the most blue-shifted components. Thus, we rule out the possibility of a small-scale expanding shell as a kinematical model of the blue-shifted maser features J–M.

Brand et al. (2003) proposed three possible mechanisms to account for the velocity drift of the maser emission: a rotating circumstelar disk, acceleration/deceleration of the jets, or a precession of the jets. According to our discussion, the most plausible explanation for the proper motions, the radial-velocity distribution, and velocity drifts of the maser features is collimated bipolar jets along the east–west direction. Thus, the origin of the velocity shift would be deceleration (because

the radial velocity of the blue-shifted features became closer to the systemic velocity) or precession of the jets.

To distinguish between possible kinematic models, proper-motion measurements of red-shifted components located at the eastern end of the maser feature distributions would be crucial. In addition, further high-resolution observations of centimeter to submillimeter continuum emission as well as near- and mid-infrared observations of the central YSO and collimated jets, if they are associated, would help to reveal the overall circumstellar structure of this source with accuracies of much better than 0.″1.

5. Conclusion

In this paper, we have presented the results of multi-epoch VLBI astrometry with VERA of the 22 GHz H_2O masers associated with IRAS 22198+6336 in L 1204 G. Using the absolute positions of a total of 26 maser spots that were detected in at least three observing sessions, we derived the annual parallax of IRAS 22198+6336 to be 1.309 ± 0.047 mas, corresponding to the distance of 764 ± 27 pc from the Sun. This is the most accurate distance to L 1204 G with an uncertainty of only 4%.

Because the newly derived distance is closer than those well adopted in the previous literature (910 pc or 1.3 kpc), the bolometric luminosity of IRAS 22198+6336 should be significantly reduced. According to the SED of IRAS 22198+6336, the bolometric luminosity and the total mass of IRAS 22198+6336 were refined to be $450\,L_\odot$ and $7\,M_\odot$, respectively. These values are not consistent with a massive YSO, but are in agreement with an intermediate-mass YSO. We confirmed that IRAS 22198+6336 would be a deeply embedded intermediate-mass YSO analogous to a low-mass Class 0 source (Sánchez-Monge et al. 2008).

Together with the annual parallax, we measured the absolute proper motions of the H_2O masers. We discussed several kinematical models of the circumstellar gas, such as a small-scale expanding shell, collimated jets, or a rotating disk. We proposed that the distributions, proper motions, and the previously reported velocity drifts (Valdettaro et al. 2002; Brand et al. 2003) of the maser features associated with IRAS 22198+6336 are consistent with the collimated bipolar jets, and possibly a rotating disk perpendicular to them.

IRAS 22198+6336 is one of the rare sources in the very early stage of intermediate-mass YSOs. Therefore, further high-resolution and high-sensitivity observations of the continuum emission from centimeter to submillimeter wavelength, particularly with the future interferometers, such as EVLA and ALMA, and the proper-motion measurements of the H_2O masers and continuum sources will be essential to reveal the kinematics and more detailed properties of IRAS 22198+6336, which will contribute to our understanding of very early stage of intermediate-mass star-formation processes.

We thank an anonymous referee for valuable comments and suggestions. We also thank Guillem Anglada and Carlos Carrasco-Gonzalez for providing us with information on the VLA observations of IRAS 22198+6336. We are grateful to the staff of all the VERA stations for their assistance in observations. TH is financially supported by Grant-in-Aids for Scientific Research from The Ministry of Education, Culture, Sports, Science and Technology (13640242, 16540224, and 20740112).

References

Anglada, G. 1995, Rev. Mexicana Astron. Astrofis. Ser. Conf., 1, 67
Brand, J., Cesaroni, R., Comoretto, G., Felli, M., Palagi, F., Palla, F., & Valdettaro, R. 2003, A&A, 407, 573
Chikada, Y., et al. 1991, in Frontiers of VLBI, ed. H. Hirabayashi, M. Inoue, & H. Kobayashi (Tokyo: Universal Academy Press), 79
Claussen, M. J., Marvel, K. B., Wootten, A., & Wilking, B. A. 1998, ApJ, 507, L79
Crampton, D., & Fisher, W. A. 1974, Publ. Dom. Astrophys. Obs., 14, 283
Dame, T. M., et al. 1987, ApJ, 322, 706
Dehnen, W., & Binney, J. J. 1998, MNRAS, 298, 387
de Zeeuw, P. T., Hoogerwerf, R., de Bruijne, J. H. J., Brown, A. G. A., & Blaauw, A. 1999, AJ, 117, 354
Edris, K. A., Fuller, G. A., & Cohen, R. J. 2007, A&A, 465, 865
Fukui, Y. 1989, in Low Mass Star Formation and Pre-Main Sequence Objects, ed. B. Reipurth (Garching: ESO), 95
Furuya, R. S., Kitamura, Y., Wootten, H. A., Claussen, M. J., Saito, M., Marvel, K. B., & Kawabe, R. 2000, ApJ, 542, L135
Hachisuka, K., et al. 2006, ApJ, 645, 337
Hirota, T., et al. 2007, PASJ, 59, 897
Hirota, T., et al. 2008, PASJ, 60, 37
Honma, M., et al. 2003, PASJ, 55, L57
Honma, M., et al. 2007, PASJ, 59, 889
Honma, M., et al. 2008a, PASJ, 60, 935
Honma, M., Tamura, Y., & Reid, M. J. 2008b, PASJ, 60, 951
Iguchi, S., Kurayama, T., Kawaguchi, N., & Kawakami, K. 2005, PASJ, 57, 259
Imai, H., et al. 2007, PASJ, 59, 1107
Jenness, T., Scott, P. F., & Padman, R. 1995, MNRAS, 276, 1024
Kawaguchi, N., Sasao, T., & Manabe, S. 2000, Proc. SPIE, 4015, 544
Loinard, L., Mioduszewski, A. J., Rodríguez, L. F., González, R. A., Rodríguez, M. I., & Torres, R. M. 2005, ApJ, 619, L179
Loinard, L., Torres, R. M., Mioduszewski, A. J., & Rodríguez, L. F. 2008, ApJ, 675, L29
Loinard, L., Torres, R. M., Mioduszewski, A. J., Rodríguez, L. F., González-Lópezlira, R. A., Lachaume, R., Vázquez, V., & González, E. 2007, ApJ, 671, 546
Lombardi, M., Lada, C. J., & Alves, J. 2008, A&A, 480, 785
Menten, K. M., Reid, M. J., Forbrich, J., & Brunthaler, A. 2007, A&A, 474, 515
Migenes, V., et al. 1999, ApJS, 123, 487
Molinari, S., Brand, J., Cesaroni, R., & Palla, F. 1996, A&A, 308, 573
Moscadelli, L., Testi, L., Furuya, R. S., Goddi, C., Claussen, M., Kitamura, Y., & Wootten, A. 2006, A&A, 446, 985
Palla, F., Brand, J., Cesaroni, R., Comoretto, G., & Felli, M. 1991, A&A, 246, 249
Patel, N. A., Greenhill, L. J., Herrnstein, J., Zhang, Q., Moran, J. M., Ho, P. T. P., & Goldsmith, P. F. 2000, ApJ, 538, 268
Perryman, M. A. C., et al. 1997, A&A, 323, L49

Petrov, L., Kovalev, Y. Y., Fomalont, E., & Gordon, D. 2005, AJ, 129, 1163
Reid, M. J. 1993, ARA&A, 31, 345
Reid, M. J., & Brunthaler, A. 2004, ApJ, 616, 872
Sánchez-Monge, Á., Palau, A., Estalella, R., Beltrán, M. T., & Girart, J. M. 2008, A&A, 485, 497
Sandstrom, K. M., Peek, J. E. G., Bower, G. C., Bolatto, A. D., & Plambeck, R. L. 2007, ApJ, 667, 1161
Sato, M., et al. 2007, PASJ, 59, 743
Sato, M., et al. 2008, PASJ, 60, 975
Stahler, S. W., & Palla, F. 2004, The Formation of Stars (Weinheim: Wiley-VCH)
Szymczak, M., Hrynek, G., & Kus, A. J. 2000, A&AS, 143, 269
Tafalla, M., Bachiller, R., & Martín-Pintado, J. 1993, ApJ, 403, 175
Tofani,G., Felli,M., Taylor, G. B., & Hunter, T. R. 1995, A&AS, 112, 299
Torrelles, J. M., et al. 2001, Nature, 411, 277
Torrelles, J. M., et al. 2003, ApJ, 598, L115
Torres, R. M., Loinard, L., Mioduszewski, A. J., & Rodríguez, L. F. 2007, ApJ, 671, 1813
Ulich, B. L., & Haas, R. W. 1976, ApJS, 30, 247
Valdettaro, R., Palla, F., Brand, J., Cesaroni, R., Comoretto, G., Felli, M., & Palagi, F. 2002, A&A, 383, 244
Wilking, B. A., Mundy, L. G., Blackwell, J. H., & Howe, J. E. 1989, ApJ, 345, 257
Wouterloot, J. G. A., & Brand, J. 1989, A&AS, 80, 149
Yonekura, Y., Dobashi, K., Mizuno, A., Ogawa, H., & Fukui, Y. 1997, ApJS, 110, 21